

# Exceptional nodal rings emerging in spinful Rice-Mele chains

E. S. Ma and Z. Song\*

*School of Physics, Nankai University, Tianjin 300071, China*

The Weyl exceptional nodal lines usually occur in 3D topological semimetals, but also emerge in the parameter space of 1D systems. In this work, we study the impact of dissipation on the nodal ring in a 3D topological semimetal. We find that the energy spectrum becomes fully complex in the presence of dissipation, and the original nodal ring is split into two exceptional rings. We introduce a vortex field in the momentum space, which is generated from the spectrum, to characterize the topology of the exceptional rings. This provides a clear physical picture of the topological structure. The two exceptional rings act as two vortex filaments of a free vortex flow with opposite circulations. In this context, the 3D topological semimetal is the boundary separating two quantum phases identified by two configurations of exceptional rings. We also propose a 1D model that has the same topological feature in the parameter space. It provides a simple way to measure the topological invariant in a low-dimensional system. Numerical simulations indicate that the topological invariant is robust under the random perturbations of the system parameters.

## I. INTRODUCTION

The search for new quantum phases of matter is a central theme in modern condensed-matter physics. The emergence of topological materials counts among the most fascinating discoveries in the field. Topological quantum states have attracted immense attention in recent years since they produce fundamentally new physical phenomena and have potential applications in novel devices. Their unique electronic structure hosts exotic phases such as topological insulators and Weyl semimetals. Research on these topics has rapidly evolved from theoretical proposals to material synthesis and characterization. One particularly intriguing direction is the realization of topological nodal-line semimetals (NLSMs) [1], in which the conduction and valence bands touch along continuous lines or loops within the three-dimensional Brillouin zone (BZ). In parallel, it has been proposed that there exists Weyl exceptional ring in a non-Hermitian system, which is characterized by both a quantized Chern number and a quantized Berry phase [2]. On the other hand, the objects of study have expanded beyond electronic systems to include non-electronic counterparts such as mechanic [3, 4], acoustic [5, 6], photonic [7–9], and ultracold atomic systems [10–14].

A genuine topological insulator or semimetal is at least two dimensional, which supports topological invariants, such as Chern number and quantized Berry flux. However, topological characterization can be demonstrated in one-dimensional systems. This allows the simplification of topology detection. A prototype example is the Rice-Mele (RM) model [15]. It is well known that adiabatic charge pumping in the RM model is quantized when the system parameters vary slowly with time along a loop lines via a chain system [16–22].

In this work, we study a non-Hermitian variant of a 3D topological semimetal and its connection to 1D systems.

We find that the energy spectrum of a 3D topological semimetal becomes fully complex and the original nodal ring is split into two exceptional rings in the presence of dissipation. Unlike the nodal loop in the original Hermitian system, where the topological features are characterized by a vector field based on the Berry curvature of the energy band, the topological features of the exceptional nodal loop are characterized by a vector field based on the complex spectrum. Furthermore, we show that the exceptional rings in a 3D topological semimetal correspond to vortex filaments of a free vortex flow. In addition, we propose a 1D RM ladder as a low-dimensional counterpart of the 3D model. This allows us to establish an experimental scheme to measure the winding number. This scheme provides a simple way since only measurements of single energy levels are needed, rather than those of a whole energy band. Numerical simulations indicate that the topological invariant is robust under random perturbations of the system parameters, which break the translational symmetry.

The rest of the paper is organized as follows. In Sec. IV A, we begin by introducing the Hamiltonian, its symmetries, and solutions. In Sec. III, we demonstrate that the exceptional rings in a 3D topological semimetal correspond to a vortex field in momentum space, which is generated from the complex spectrum. On the basis of these results, in Sec. IV, we propose a 1D RM model that has the same topological features in the parameter space. This model provides a simple way to measure topological invariants in a low-dimensional system. Following these formulations, in Sec. V, numerical calculations are used to compare the results obtained from a perfect system with those from a system with disorder perturbations. Finally, Sec. VI summarizes our findings. Some detailed derivations are given in the Appendix.

## II. MODEL AND EXCEPTIONAL RINGS

Our starting point is a non-Hermitian system derived from a three-dimensional Hermitian model of a nodal-

\* [songtc@nankai.edu.cn](mailto:songtc@nankai.edu.cn)

ring semimetal. The Hamiltonian in the momentum space has the following form

$$H(\mathbf{k}) = k_x s_x + k_y \tau_y s_y + k_z s_z + m \tau_x s_x, \quad (1)$$

where  $\tau_i$  and  $s_i$  ( $i = x, y, z$ ) are Pauli matrices for two isospin degrees of freedom. The explicit matrix form of the Hamiltonian is

$$H(\mathbf{k}) = \begin{pmatrix} k_z & k_x & 0 & -k_y + m \\ k_x & -k_z & k_y + m & 0 \\ 0 & k_y + m & k_z & k_x \\ -k_y + m & 0 & k_x & -k_z \end{pmatrix}, \quad (2)$$

which has been systematically studied in Ref. [23] in the case with real  $m$ . In this work, we extend the model to a non-Hermitian one by taking complex  $m$ , i.e.,

$$m = \alpha + i\beta. \quad (3)$$

No matter  $m$  is real or complex,  $H(\mathbf{k})$  is chirally symmetric, because

$$\Lambda H(\mathbf{k}) \Lambda^{-1} = -H(\mathbf{k}), \quad (4)$$

where the matrix  $\Lambda$  is

$$\Lambda = \begin{pmatrix} 0 & 0 & 0 & i \\ 0 & 0 & -i & 0 \\ 0 & i & 0 & 0 \\ -i & 0 & 0 & 0 \end{pmatrix}. \quad (5)$$

The eigen energy of  $H(\mathbf{k})$  is

$$\varepsilon_{\mu,\nu} = \mu \sqrt{k_z^2 + \left( \sqrt{k_x^2 + k_y^2} + \nu m \right)^2}, \quad (6)$$

with  $\mu, \nu = \pm$ , in associated with the corresponding eigenstate

$$|\psi_{\mu,\nu}\rangle = \begin{pmatrix} k_x^2 + (k_y - m) \left( k_y - \nu \sqrt{k_x^2 + k_y^2} \right) \\ k_x (\varepsilon_{\mu,\nu} - k_z) \\ k_x (m^2 - k_y^2 - \xi) / 2m \\ (k_z - \varepsilon_{\mu,\nu}) \left[ (k_y + m)^2 + \xi \right] / 2m \end{pmatrix}, \quad (7)$$

where  $\xi = k_x^2 + k_z^2 - \varepsilon_{\mu,\nu}^2$ . Obviously the nodal lines occur at  $\mathbf{k} = \mathbf{k}_c$ , which is determined by the equation  $\varepsilon_{\mu,+}(\mathbf{k}_c) = 0$  or  $\varepsilon_{\mu,-}(\mathbf{k}_c) = 0$ . Here we only consider the case with  $\alpha \geq 0$  for simplicity. Similar conclusions can be obtained for  $\alpha < 0$ . Then the nodal line obeys the equations

$$\sqrt{k_{cx}^2 + k_{cy}^2} = \alpha, k_{cz} = \pm \beta, \quad (8)$$

which represent a pair of concentric circles of radius  $\alpha$  in three-dimensional momentum space. The distance between these two circles is  $2|\beta|$ . Subsequently, we have  $\xi_c = k_x^2 + \beta^2$ . The zero-energy eigenstates have the form

$$|\psi_{\mu,-}(\mathbf{k}_c)\rangle = \begin{pmatrix} -i(\alpha + k_{cy}) \\ -k_{cx}k_{cz}/\beta \\ ik_{cx} \\ (\alpha + k_{cy})k_{cz}/\beta \end{pmatrix}, \quad (9)$$

and we have

$$|\psi_{+,-}(\mathbf{k}_c)\rangle = |\psi_{-,-}(\mathbf{k}_c)\rangle, \quad (10)$$

which is the coalescing state. However, for  $\beta = 0, \varepsilon_{\mu,\nu} = 0$  gives

$$\sqrt{k_{cx}^2 + k_{cy}^2} = \alpha, k_{cz} = 0, \quad (11)$$

and the corresponding zero-energy eigenstates can be expressed as

$$|\psi_{+,-}(\mathbf{k}_c)\rangle = \begin{pmatrix} k_{cy} + \alpha \\ 0 \\ -k_{cx} \\ 0 \end{pmatrix}, \quad (12)$$

$$|\psi_{-,-}(\mathbf{k}_c)\rangle = \begin{pmatrix} 0 \\ -k_{cx} \\ 0 \\ k_{cy} + \alpha \end{pmatrix}, \quad (13)$$

we have

$$\langle \psi_{+,-}(\mathbf{k}_c) | \psi_{-,-}(\mathbf{k}_c) \rangle = 0. \quad (14)$$

which indicate that the nodal ring is split into two exceptional rings by nonzero  $\beta$ . In Fig. 1 (a1), (b1), and (c1) we present the schematic diagram for the exceptional rings at different  $\beta$ . In the following, we investigate the topological characters of the exceptional rings.

### III. EXCEPTIONAL RINGS AS VORTEX FILAMENTS

For the Hermitian case, the topology of the nodal ring is characterized by invariant quantities, which are abstracted from the set of eigenstates  $\{|\psi_{\mu,\nu}\rangle\}$  at  $\beta = 0$ . Unlike the Hermitian case, the topology of the nodal ring is characterized by the invariant quantity, which is abstracted from the spectrum  $\{\varepsilon_{\mu,\nu}\}$ . Based on the previous study in Refs. [24, 25], we introduce a vector field defined as follows

$$\mathbf{P} = \nabla_{\mathbf{k}} (\phi_+ + \phi_-), \quad (15)$$

where  $\phi_{\pm}$  is the argument of  $\varepsilon_{\mu,\pm}^2$ , respectively, i.e.,

$$\varepsilon_{\mu,\pm}^2 = |\varepsilon_{\mu,\pm}^2| e^{i\phi_{\pm}}. \quad (16)$$

In the Appendix, we show that field  $\mathbf{P}$  describes a free vortex flow induced by the exceptional rings acting as vortex filaments. In general, vortex filaments are idealized, infinitesimally thin lines of concentrated vorticity,

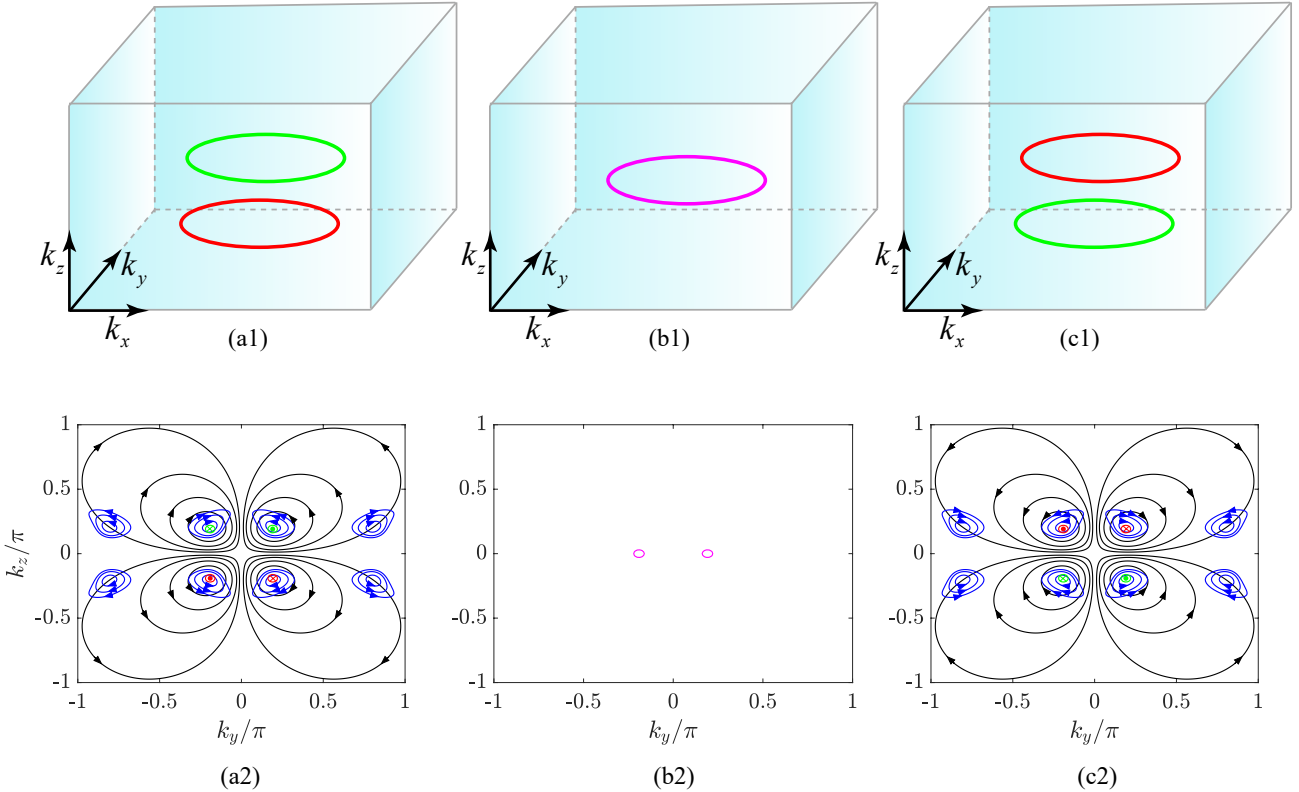


FIG. 1. Schematic of the exceptional rings described by Eq. (8) in three-dimensional momentum space, together with the gradient field of the eigenenergy argument defined in the Eq. (15) and the analogous field of the RM model under the parameter transformation of Eq. (36). Panels (a1), (b1) and (c1) correspond to  $\alpha = 0.6$  and  $\beta = 0.6, 0$ , and  $-0.6$ , respectively. Panels (a2), (b2) and (c2) show the corresponding field lines of  $\mathbf{P}$  (black) and the approximate field lines of the RM model (blue) near the exceptional points in the  $k_y - k_z$  plane; arrows indicate the directions. For the semimetal model, the field  $\mathbf{P}$  forms a free vortex flow whose circulation follows the right-hand screw rule, marked by green or red circles.

while a free vortex flow describes circular motion where fluid velocity decreases inversely with radius. This provides a clear physical picture of the topological structure.

We introduce the winding number to characterize the topology of the EP rings, which is defined as

$$w = \oint_{\mathcal{L}} \mathbf{P} \cdot \frac{d\mathbf{k}}{2\pi}, \quad (17)$$

where  $\mathcal{L}$  denotes an arbitrary closed loop in the momentum space. Detailed derivations in Appendix A show that the winding number is an integer with possible values  $(0, \pm 1)$ , determined by the geometric relationship between the closed loop  $\mathcal{L}$  and the two exceptional rings. The two exceptional rings act as two vortex filaments of a free vortex flow carrying opposite circulations. When the parameter  $\beta$  passes through zero, the two exceptional rings swap places. In this context, the 3D Hermitian topological semimetal is the boundary separating two quantum phases identified by two configurations of exceptional rings. This is consistent with the fact that  $|\psi_{\mu,\nu}(\mathbf{k}_c)\rangle$  is non-analytic at  $\beta = 0$ . We demonstrate the contour of  $\mathbf{P}$  in Fig. 1 (a2), (b2) and (c2) for several

representative configurations of exceptional rings.

#### IV. RICE-MELE CHAIN

In the previous sections, we investigated the non-Hermitian semimetal using the Hamiltonian in momentum space. However, the Hamiltonian  $H(\mathbf{k})$  given in Eq. (2) is not the periodic function of  $\mathbf{k}$ , based on which one cannot obtain a 3D lattice system. On the other hand, the corresponding 3D lattice system probably consists of somewhat complicated hopping and on-site terms. This would be an obstacle to fabricating the sample and detecting the topological features in experiments. In this section, we propose a spinful RM chain model and show that it has similar topological features in parameter space. We also propose an experimental scheme to measure the topological index.

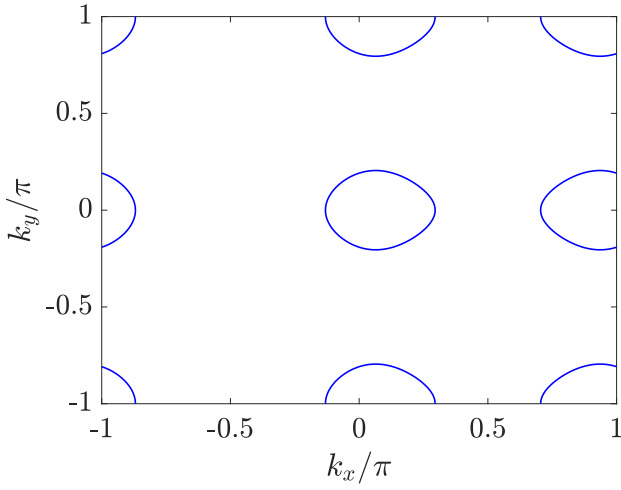


FIG. 2. Exceptional rings viewed in the  $k_x - k_y$  plane, given by Eq. (38) with  $\alpha = \beta = 0.6$ . Each loop represent a pair of exceptional rings corresponding  $\sin k_{cz} = \pm\beta$ .

### A. Hamiltonian and solution

Consider a 1D RM model on a  $2N$  lattice with spin-orbit coupling. The Hamiltonian is

$$H = \sum_{\sigma=\uparrow,\downarrow} H_\sigma + H_{\text{so}}, \quad (18)$$

where the coupling-free part is

$$H_\sigma = \sum_{j=1}^N \sum_{\sigma=\uparrow,\downarrow} \left[ (\delta - 1) c_{2j-1,\sigma}^\dagger c_{2j,\sigma} + c_{2j,\sigma}^\dagger c_{2j+1,\sigma} + \text{h.c.} \right] - \sum_{j=1}^{2N} \sum_{\sigma=\uparrow,\downarrow} (-1)^{j+\sigma} V c_{j,\sigma}^\dagger c_{j,\sigma}, \quad (19)$$

and the spin-orbit coupling term is

$$H_{\text{so}} = \lambda \sum_{j=1}^N \sum_{\sigma=\uparrow,\downarrow} \left( c_{2j-1,\sigma}^\dagger c_{2j,-\sigma} + \text{h.c.} \right). \quad (20)$$

Here,  $c_{j,\sigma}^\dagger (c_{j,\sigma})$  is the fermion creation (annihilation) operator at the  $j$ th site.  $H_\uparrow$  and  $H_\downarrow$  represent two independent RM models with opposite spin, and the on-site potential  $V$  is spin-dependent with  $(-1)^\uparrow = -(-1)^\downarrow = 1$ . The spin-orbit coupling strength is  $\lambda$ . It is equivalent to a spinless fermion ladder system, which is experimentally realizable in waveguide arrays or acoustic systems [26–28]. With periodic boundary conditions, i.e.,  $c_{2N+1,\sigma} = c_{1,\sigma}$ , the Hamiltonian possesses translational symmetry. Then, employing Fourier transformation as follows

$$\begin{pmatrix} c_{2j-1,\uparrow} \\ c_{2j,\uparrow} \\ c_{2j-1,\downarrow} \\ c_{2j,\downarrow} \end{pmatrix} = \frac{e^{-ikj}}{\sqrt{N}} \begin{pmatrix} a_{k,\uparrow} \\ b_{k,\uparrow} \\ b_{k,\downarrow} \\ a_{k,\downarrow} \end{pmatrix}, \quad (21)$$

where  $k = 2n\pi/N$  ( $n = 0, 1, \dots, N-1$ ), the Hamiltonian can be written as

$$H = \sum_{2\pi > k \geq 0} \Psi_k^\dagger h_k \Psi_k. \quad (22)$$

Here, we define the operator vector  $\Psi_k^\dagger = (a_{k,\uparrow}^\dagger, b_{k,\uparrow}^\dagger, a_{k,\downarrow}^\dagger, b_{k,\downarrow}^\dagger)$ , and the Hamiltonian matrix takes the form

$$h_k = \begin{pmatrix} V & \zeta & \lambda & 0 \\ \zeta^* & -V & 0 & \lambda \\ \lambda & 0 & V & \zeta^* \\ 0 & \lambda & \zeta & -V \end{pmatrix}, \quad (23)$$

with the momentum-dependent factor  $\zeta = \delta - 1 + e^{ik}$ .

As with the Hamiltonian in Eq. (4), the Bloch Hamiltonian satisfies

$$S h_k S^{-1} = -h_k, \quad (24)$$

where the unitary operator

$$S = \begin{pmatrix} 0 & 0 & 0 & -1 \\ 0 & 0 & 1 & 0 \\ 0 & 1 & 0 & 0 \\ -1 & 0 & 0 & 0 \end{pmatrix}, \quad (25)$$

implements the chiral symmetry. Consequently, the spectrum is symmetric about zero. The spectrum of  $h_k$  consists of four branches

$$\epsilon_{\mu,\nu} = \mu \sqrt{(\lambda + \nu R)^2 + \sin^2 k}, \quad (26)$$

with band indices  $\mu = \pm$ ,  $\nu = \pm$ , and the  $k$ -dependent factor

$$R = \sqrt{V^2 + (\delta - 1 + \cos k)^2}. \quad (27)$$

Similarly, with the complex spin-orbit coupling defined as

$$\lambda = \alpha + i\beta, \quad (28)$$

the corresponding eigenstates of  $h_k$  are given by

$$|\phi_{\mu,\nu}\rangle = \begin{pmatrix} \lambda^2 [\zeta^* (V + \epsilon_{\mu,\nu}) + \zeta (\epsilon_{\mu,\nu} - V)] \\ \Gamma^2 - \lambda^2 [(V + \epsilon_{\mu,\nu})^2 + \zeta^2] \\ \lambda (\lambda^2 \zeta - \zeta^* \Gamma) \\ \lambda [\Gamma (V - \epsilon_{\mu,\nu}) - \lambda^2 (V + \epsilon_{\mu,\nu})] \end{pmatrix}, \quad (29)$$

with the  $k$ -dependent factor

$$\Gamma = \zeta \zeta^* + V^2 - \epsilon_{\mu,\nu}^2. \quad (30)$$

Accordingly, the exceptional point condition  $\epsilon_{\mu,\nu} = 0$  leads, for  $\alpha > 0$ , to

$$\begin{aligned} \sqrt{V_c^2 + (\delta_c - 1 + \cos k_c)^2} &= \alpha, \\ \sin k_c &= \pm\beta. \end{aligned} \quad (31)$$

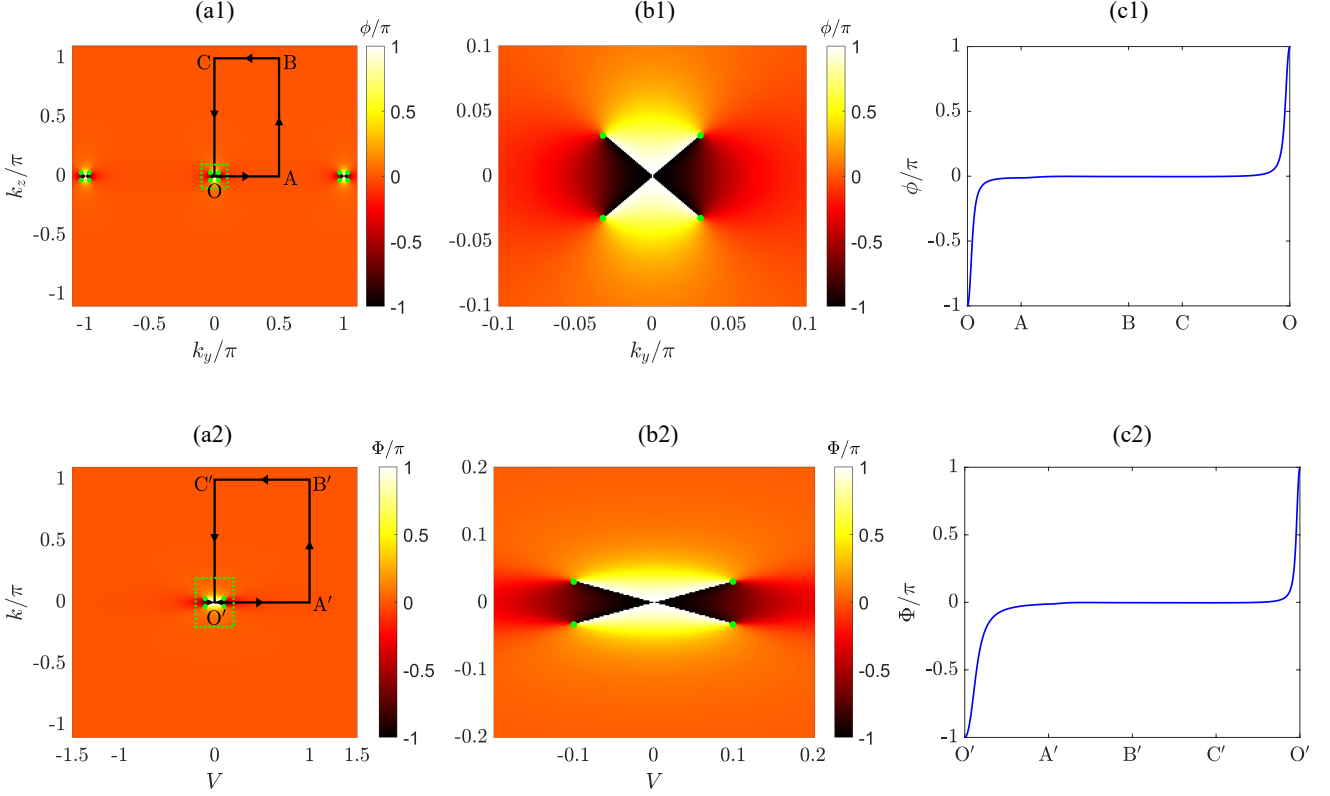


FIG. 3. Contour plots of  $\phi = \phi_+ + \phi_-$  from Eq. (16) ( $\Phi = \Phi_+ + \Phi_-$  from Eq. (43)) on the  $k_y - k_z$  ( $V - k$ ) plane with  $k_x = 0$  ( $\delta = 0$ ) and  $\alpha = \beta = 0.1$ . Green dots mark the exceptional points, symmetric about both axes. O ( $O'$ ) denotes the origin. Black rectangles in (a1) and (a2) encircle single exceptional points; (c1) and (c2) show the corresponding values along the arrows, yielding a winding number of 1. Panels (b1) and (b2) magnify the regions within the green-dashed frames of (a1) and (a2).

These equations define two circles of radius  $\alpha$  with distinct centers in the  $(\delta, V)$  plane, corresponding to different values of  $k$ .

For  $v = -$ , the zero-energy eigenstates are given by

$$|\phi_{\mu,-}^c\rangle = \begin{pmatrix} V_c \sin k_c / \beta \\ \alpha + (\delta - 1 + \cos k_c) \sin k_c / \beta \\ -(\alpha \sin k_c / \beta + \delta - 1 + \cos k_c) \end{pmatrix}. \quad (32)$$

At the exceptional ring, the two states  $|\phi_{+,-}^c\rangle$  and  $|\phi_{-,-}^c\rangle$  coalesce. In the limit  $\beta = 0$ , the condition  $\epsilon_{\mu,\nu} = 0$  reduces to

$$\begin{aligned} \sqrt{V_c^2 + (\delta_c - 1 + \cos k_c)^2} &= \alpha, \\ \sin k_c &= 0, \end{aligned} \quad (33)$$

the corresponding zero-energy eigenstates can be expressed as

$$|\phi_{+,-}^c\rangle = \begin{pmatrix} -\zeta_c \\ V_c \\ 0 \\ \alpha \end{pmatrix}, \quad |\phi_{-,-}^c\rangle = \begin{pmatrix} -V_c \\ -\zeta_c \\ \alpha \\ 0 \end{pmatrix}, \quad (34)$$

with  $\zeta_c = \delta_c - 1 + \cos k_c$ . These two states are orthogonal

$$\langle \phi_{+,-}^c | \phi_{-,-}^c \rangle = 0. \quad (35)$$

The exceptional point structure of the RM model resembles that of the Hamiltonian  $H(\mathbf{k})$  discussed above.

## B. Connection with 3D model

In this subsection, we establish the connection between the RM model and the matrix  $H(\mathbf{k})$ , given in Eq. (2), enabling us to demonstrate the obtained results within the RM model. Under the parameter transformation

$$(\delta, V, k) \rightarrow (\sin k_x, \sin k_y, k_z), \quad (36)$$

the Hamiltonian takes the form

$$h_{\mathbf{k}} = \begin{pmatrix} \sin k_y & \zeta & \lambda & 0 \\ \zeta^* & -\sin k_y & 0 & \lambda \\ \lambda & 0 & \sin k_y & \zeta^* \\ 0 & \lambda & \zeta & -\sin k_y \end{pmatrix}, \quad (37)$$

where  $\zeta = \sin k_x - 1 + e^{ik_z}$ , rendering the system periodic in 3D momentum space. Consequently, the  $\phi_{\pm}$  and

**P** fields are obtained as periodic functions in the 3D momentum space. The singularities of these fields constitute exceptional loops satisfying

$$\begin{aligned} \sqrt{\sin^2 k_{cy} + (\sin k_{cx} - 1 + \cos k_{cz})^2} &= \alpha, \\ \sin k_{cz} &= \pm\beta. \end{aligned} \quad (38)$$

In contrast to the circular exceptional rings of  $H(\mathbf{k})$ , those in the RM model exhibit a more complex geometry. Fig. 1 shows the field lines of **P** for the RM model, compared with those for  $H(\mathbf{k})$ . In Fig. 2 we plot the exceptional loops for a set of representative parameters in the  $k_x - k_y$  plane, which appear in pairs at opposite values of  $k_{cz}$ . In Fig. 3(a1) we plot the field  $\phi = \phi_+ + \phi_-$  in the  $k_y - k_z$  plane with zero  $k_{cx}$ .

We can see that  $H(\mathbf{k})$  can be regarded as the effective Hamiltonian of  $h_{\mathbf{k}}$  according to the following analysis. We note that in the vicinity of  $(k_x, k_y, k_z) = (0, 0, 0)$ , the Hamiltonian can be approximated as

$$\bar{h}_{\mathbf{k}} = \begin{pmatrix} k_y & k_x + ik_z & \lambda & 0 \\ k_x - ik_z & -k_y & 0 & \lambda \\ \lambda & 0 & k_y & k_x - ik_z \\ 0 & \lambda & k_x + ik_z & -k_y \end{pmatrix}, \quad (39)$$

by performing a Taylor series expansion. Furthermore, upon introducing the unitary transformation

$$U = \frac{1}{2} \begin{pmatrix} -i & 1 & i & 1 \\ 1 & -i & 1 & i \\ 1 & i & 1 & -i \\ i & 1 & -i & 1 \end{pmatrix}, \quad (40)$$

$\bar{h}_{\mathbf{k}}$  is transformed to

$$\begin{pmatrix} k_z & k_x & 0 & -k_y + \lambda \\ k_x & -k_z & k_y + \lambda & 0 \\ 0 & k_y + \lambda & k_z & k_x \\ -k_y + \lambda & 0 & k_x & -k_z \end{pmatrix}, \quad (41)$$

which coincides with  $H(\mathbf{k})$  in Eq. (2) under the replacement  $\lambda \rightarrow m$ .

On the other hand, taking the operator vector

$$\Psi_{\mathbf{k}}^\dagger = (a_{\mathbf{k},\uparrow}^\dagger \ b_{\mathbf{k},\uparrow}^\dagger \ a_{\mathbf{k},\downarrow}^\dagger \ b_{\mathbf{k},\downarrow}^\dagger), \quad (42)$$

the 3D Hamiltonian in real space can be obtained from  $\sum_{\mathbf{k}} \Psi_{\mathbf{k}}^\dagger h_{\mathbf{k}} \Psi_{\mathbf{k}}$ . However, the real-space Hamiltonian describes a 3D lattice system with somewhat complicated hopping and on-site terms. Therefore, in what follows we consider the problem using a 1D lattice system.

### C. Topology in parameter space

Now we turn to the topology of the RM model in the parameter space  $(\delta, V, k)$ . Similarly, based on the spectrum in Eq. (26), one can define the arguments of eigenenergies through the relation

$$\epsilon_{+,\pm}^2 = |\epsilon_{+,\pm}^2| e^{i\Phi_{\pm}}, \quad (43)$$

which gives

$$\tan \Phi_{\pm} = \frac{2\beta(\alpha \pm R)}{\sin^2 k + (\alpha \pm R)^2 - \beta^2}. \quad (44)$$

In the case of small  $k$ , we have

$$\tan \Phi_{\pm} \approx \frac{2\beta(\alpha \pm R)}{k^2 + (\alpha \pm R)^2 - \beta^2}, \quad (45)$$

$$R \approx \sqrt{V^2 + \delta^2}, \quad (46)$$

which is identical to the expression  $\phi_{\pm}$  in the Appendix by  $R \rightarrow \rho$  and  $k \rightarrow k_z$ . Therefore, the topological feature for  $H(\mathbf{k})$  can be simulated via a 1D RM chain in the parameter space. In Fig. 3(a2) we plot the field  $\Phi = \Phi_+ + \Phi_-$  for comparison with that in 3D momentum space.

From these plots, we note that both fields  $\phi$  and  $\Phi$  remain constant in regions far from the exceptional points (EPs). Consequently, one can construct a loop containing segments that do not contribute to the path integral, which simplifies the determination of the winding number. For instance, we can take a rectangular as a loop in the 3D momentum space  $(k_x, k_y, k_z)$ , which contains four segments: (I)  $(0, 0, 0) \rightarrow (0, \pi/2, 0)$ ; (II)  $(0, \pi/2, 0) \rightarrow (0, \pi/2, \pi)$ ; (III)  $(0, \pi/2, \pi) \rightarrow (0, 0, \pi)$ ; (IV)  $(0, 0, \pi) \rightarrow (0, 0, 0)$ . Analytical analysis indicates that for  $\alpha \approx \beta \rightarrow 0$ , the path integrals along (II) and (III) are approximately zero. Then the corresponding winding number is

$$\begin{aligned} w &= \int_0^{\pi/2} P_y(0, k_y, 0) \frac{dk_y}{2\pi} + \int_{\pi}^0 P_z(0, 0, k_z) \frac{dk_z}{2\pi} \\ &= \frac{\phi(0, \pi/2, 0) - \phi(0, 0, \pi)}{2\pi} + 1. \end{aligned} \quad (47)$$

which can be directly obtained from the spectrum of the 3D lattice  $\sum_{\mathbf{k}} \Psi_{\mathbf{k}}^\dagger h_{\mathbf{k}} \Psi_{\mathbf{k}}$ . Alternatively, we can perform a similar procedure for a RM chain, by replacing  $\phi(k_x, k_y, k_z)$  with  $\Phi(\delta, V, k)$ . We have

$$w = \frac{\Phi(0, \pi/2, 0) - \Phi(0, 0, \pi)}{2\pi} + 1. \quad (48)$$

In practice,  $\Phi(\delta, V, 0)$  and  $\Phi(\delta, V, \pi)$  can be directly obtained from the band edges. A detailed explanation is presented in the next section. This renders the experimental measurement of the winding number feasible. To demonstrate this point, we perform numerical simulations for the finite RM chain. The results are shown in Fig. 3(c1) and are consistent with the analytical prediction.

### V. ROBUSTNESS TO PERTURBATIONS

In the previous section, we have shown that the winding number can be obtained from some special energy levels in the spectrum. Moreover, we know that the boundary conditions and slight perturbations may not affect

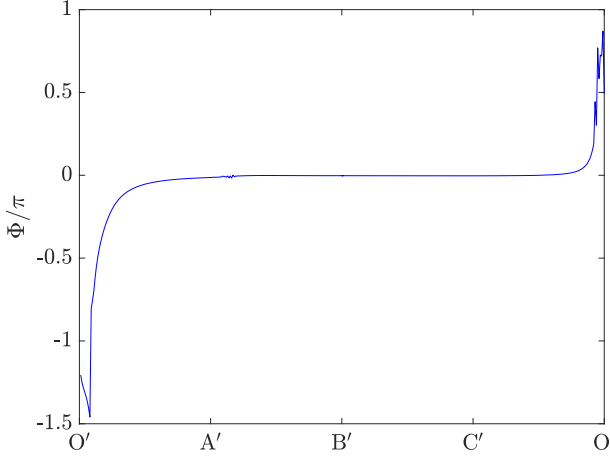


FIG. 4. Plot of  $\Phi$  extracted from the real space energy spectrum of a ring model along the black rectangle shown in Fig. 3(a2) with the perturbation described in Eq. (52); here  $k$  can be interpreted as quasi-momentum. Other parameters are  $a = 0.1$ ,  $\alpha = \beta = 0.1$ , and  $N = 200$ .

the spectrum significantly. Therefore, it is still possible to extract the winding number from the spectrum in the presence of perturbations. In this section, we investigate this scheme thoroughly.

We begin with the spectrum of the RM model in the parameter space  $(\delta, V, k)$ . From the spectrum in Eq. (26), we have

$$\epsilon_{+, \pm}^2 = (\alpha \pm R)^2 - \beta^2 + \sin^2 k + 2i\beta(\alpha \pm R), \quad (49)$$

and consequently

$$\text{Im}(\epsilon_{+,+}^2 + \epsilon_{+,-}^2) = 4\beta\alpha, \quad (50)$$

which means that the imaginary parts of  $\epsilon_{+, \pm}^2$  are symmetric with respect to the constant value  $2\beta\alpha$  (i.e.,  $\text{Im}(\epsilon_{+,+}^2) = 2\beta\alpha + R$  and  $\text{Im}(\epsilon_{+,-}^2) = 2\beta\alpha - R$ ). In addition, on the  $\delta = 0$  plane we have

$$\frac{\partial R}{\partial k} = \frac{(1 - \cos k) \sin k}{R} \geq 0 \quad (51)$$

for  $k \in [0, \pi]$ , indicating that  $\text{Im}(\epsilon_{+, \pm}^2)$  are monotonic functions of  $k$ . These features allow us to distinguish different bands and label the energy level by  $k$  according to the values of  $\text{Im}(\epsilon_{+,+}^2)$ . We presume that such features remain unchanged in the presence of perturbations even when the translational symmetry is broken. In the following, we consider a random perturbation on the on-site potentials,

$$V_j = V + \text{ran}(-a, a)_j, \quad (52)$$

where  $\text{ran}(-a, a)_j$  denotes a uniform random number in  $(-a, a)$  and  $j$  is the unit-cell index with  $j \in [1, N]$ . A

numerical simulation is performed by taking a set of random numbers  $\{V_j\}$  centered around  $V$ . Obviously, the perturbation breaks the translational symmetry even under periodic boundary conditions but preserves the chiral symmetry. If the perturbation is small enough, it is expected that the energy levels and their order slightly deviate from those in the case without perturbation.

Therefore, the winding number can still be obtained from the arguments of the eigenenergies using the method presented in Fig. 3. To verify our prediction, we performed numerical simulations on a finite system with random numbers  $\{V_j\}$ . The results are shown in Fig. 4. As illustrated, along the same loop as in Fig. 3(a2), the change in the argument is similar to that in Fig. 3(c2), with the total change approximately equal to  $2\pi$ , demonstrating the topological robustness against perturbations.

## VI. SUMMARY

In summary, we have studied the topological features of exceptional nodal rings emerging in the parameter space of a spinful Rice-Mele chain. The main contributions are twofold. First, we show that the exceptional rings in a 3D topological semimetal correspond to a vortex field in momentum space, which is generated from the complex spectrum. The two exceptional rings act as vortex filaments of a free vortex flow with opposite circulations. This finding may be extended to a class of non-Hermitian systems in the future. Second, we propose an experimental scheme to measure the winding number via a low-dimensional system. The advantage of this scheme is that only measurements of single energy levels are needed, rather than those of a whole energy band.

## ACKNOWLEDGMENTS

This work was supported by the National Natural Science Foundation of China (under Grant No. 12374461).

## APPENDIX: VORTEX FIELD $\mathbf{P}$

In this appendix, we derive the expression of field  $\mathbf{P}$  in Eq. (15) and demonstrate its features. We note that the function  $\varepsilon_{\mu, \nu}(\mathbf{k})$  has rotational symmetry about the  $k_z$  axis. It is convenient to take a cylindrical coordinate system as shown in Fig. A 1. The unit vectors along the radius  $\rho = \sqrt{k_x^2 + k_y^2}$  and the  $k_z$  axis are  $\mathbf{e}_\rho$  and  $\mathbf{e}_z$ , respectively. Then the argument given in Eq. (16) can be expressed as

$$\phi_{\pm} = \arctan \frac{2\beta(\alpha \pm \rho)}{k_z^2 + (\alpha \pm \rho)^2 - \beta^2}. \quad (\text{A } 1)$$

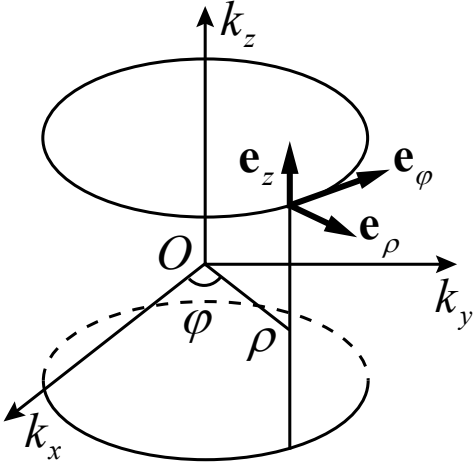


FIG. A 1. Schematic of the cylindrical coordinate system in momentum space. Here  $\rho = \sqrt{k_x^2 + k_y^2}$  is the radial distance,  $\varphi$  is the azimuthal angle, and  $(\mathbf{e}_\rho, \mathbf{e}_\varphi, \mathbf{e}_z)$  are the orthonormal basis vectors.

Accordingly, the field can be obtained as

$$\mathbf{P} = \left( \frac{\partial}{\partial \rho} \mathbf{e}_\rho + \frac{\partial}{\partial k_z} \mathbf{e}_z \right) (\phi_+ + \phi_-). \quad (\text{A } 2)$$

The explicit expression of the field is

$$\mathbf{P} = \frac{\mathbf{e}_1}{r_1} - \frac{\mathbf{e}_2}{r_2} + \frac{\mathbf{e}_3}{r_3} - \frac{\mathbf{e}_4}{r_4}, \quad (\text{A } 3)$$

where  $r_i = |\mathbf{r}_i|$  ( $i \in [1, 4]$ ) denotes the length of the vector  $\mathbf{r}_i$ , and

$$\mathbf{e}_i = \cos \theta_i \mathbf{e}_z - \sin \theta_i \mathbf{e}_\rho, \quad (\text{A } 4)$$

is the tangential unit vector with respect to  $\mathbf{r}_i/r_i$  in the radial direction. Here, the explicit expressions of  $\mathbf{r}_i$  are

$$\begin{aligned} \mathbf{r}_1 &= (\rho - \alpha) \mathbf{e}_\rho + (k_z - \beta) \mathbf{e}_z, \\ \mathbf{r}_2 &= (\rho - \alpha) \mathbf{e}_\rho + (k_z + \beta) \mathbf{e}_z, \\ \mathbf{r}_3 &= (\rho + \alpha) \mathbf{e}_\rho + (k_z + \beta) \mathbf{e}_z, \\ \mathbf{r}_4 &= (\rho + \alpha) \mathbf{e}_\rho + (k_z - \beta) \mathbf{e}_z, \end{aligned} \quad (\text{A } 5)$$

which are clearly the position vectors of the point  $\mathbf{k}$  with respect to four exceptional points  $\alpha \mathbf{e}_\rho + \beta \mathbf{e}_z$ ,  $\alpha \mathbf{e}_\rho - \beta \mathbf{e}_z$ ,  $-\alpha \mathbf{e}_\rho - \beta \mathbf{e}_z$ , and  $-\alpha \mathbf{e}_\rho + \beta \mathbf{e}_z$ , respectively. In this sense, the physical picture is clear: the  $\mathbf{P}$  field is the superposition of four free vortex flows induced by the two exceptional rings acting as vortex filaments. Accordingly, the winding number, given in Eq. (17), is expressed as

$$w = \frac{1}{2\pi} \oint_{\mathcal{L}} d(\theta_1 - \theta_2 + \theta_3 - \theta_4). \quad (\text{A } 6)$$

It accords with the expression of the form

$$\begin{aligned} w &= \oint_{\mathcal{L}} \frac{d\mathbf{k}}{2\pi i} \cdot \nabla_{\mathbf{k}} \log (\varepsilon_{+,+}^2 \varepsilon_{+,-}^2) \\ &= \oint_{\mathcal{L}} \frac{d\mathbf{k}}{2\pi i} \cdot \nabla_{\mathbf{k}} \log \det [H(\mathbf{k}) - \varepsilon(\mathbf{k}_c)], \end{aligned} \quad (\text{A } 7)$$

which appeared in the previous work [24].

---

[1] A. A. Burkov, M. D. Hook, and L. Balents, Topological nodal semimetals, *Phys. Rev. B* **84**, 235126 (2011).

[2] Y. Xu, S.-T. Wang, and L.-M. Duan, Weyl exceptional rings in a three-dimensional dissipative cold atomic gas, *Phys. Rev. Lett.* **118**, 045701 (2017).

[3] C. L. Kane and T. C. Lubensky, Topological boundary modes in isostatic lattices, *Nature Physics* **10**, 39 (2014).

[4] S. D. Huber, Topological mechanics, *Nature Physics* **12**, 621 (2016).

[5] Z. Yang, F. Gao, X. Shi, X. Lin, Z. Gao, Y. Chong, and B. Zhang, Topological acoustics, *Phys. Rev. Lett.* **114**, 114301 (2015).

[6] X. Zhang, M. Xiao, Y. Cheng, M.-H. Lu, and J. Christensen, Topological sound, *Communications Physics* **1**, 97 (2018).

[7] F. D. M. Haldane and S. Raghu, Possible realization of directional optical waveguides in photonic crystals with broken time-reversal symmetry, *Phys. Rev. Lett.* **100**, 013904 (2008).

[8] L. Lu, J. D. Joannopoulos, and M. Soljačić, Topological photonics, *Nature photonics* **8**, 821 (2014).

[9] T. Ozawa, H. M. Price, A. Amo, N. Goldman, M. Hafezi, L. Lu, M. C. Rechtsman, D. Schuster, J. Simon, O. Zilberman, and I. Carusotto, Topological photonics, *Rev. Mod. Phys.* **91**, 015006 (2019).

[10] M. Atala, M. Aidelsburger, J. T. Barreiro, D. Abanin, T. Kitagawa, E. Demler, and I. Bloch, Direct measurement of the zak phase in topological bloch bands, *Nature Physics* **9**, 795 (2013).

[11] N. Goldman, J. C. Budich, and P. Zoller, Topological quantum matter with ultracold gases in optical lattices, *Nature Physics* **12**, 639 (2016).

[12] L. Wang, M. Troyer, and X. Dai, Topological charge pumping in a one-dimensional optical lattice, *Phys. Rev. Lett.* **111**, 026802 (2013).

[13] S. Nakajima, T. Tomita, S. Taie, T. Ichinose, H. Ozawa, L. Wang, M. Troyer, and Y. Takahashi, Topological thouless pumping of ultracold fermions, *Nature Physics* **12**, 296 (2016).

[14] M. Lohse, C. Schweizer, O. Zilberman, M. Aidelsburger, and I. Bloch, A thouless quantum pump with ultracold bosonic atoms in an optical superlattice, *Nature Physics*

**12**, 350 (2016).

[15] M. J. Rice and E. J. Mele, Elementary excitations of a linearly conjugated diatomic polymer, *Phys. Rev. Lett.* **49**, 1455 (1982).

[16] R. Wang, C. Li, X. Z. Zhang, and Z. Song, Dynamical bulk-edge correspondence for degeneracy lines in parameter space, *Phys. Rev. B* **98**, 014303 (2018).

[17] R. Wang and Z. Song, Robustness of the pumping charge to dynamic disorder, *Phys. Rev. B* **100**, 184304 (2019).

[18] R. Wang, X. Z. Zhang, and Z. Song, Dynamical topological invariant for the non-hermitian rice-mele model, *Phys. Rev. A* **98**, 042120 (2018).

[19] E. Ma and Z. Song, Topological charge pumping in tetramerized kitaev chains with nodal loop in parameter space, *New Journal of Physics* **26**, 063036 (2024).

[20] D. Xiao, M.-C. Chang, and Q. Niu, Berry phase effects on electronic properties, *Rev. Mod. Phys.* **82**, 1959 (2010).

[21] J. K. Asbóth, L. Oroszlány, and A. Pályi, *A short course on topological insulators*, Vol. 919 (Springer, 2016).

[22] D. Vanderbilt, *Berry phases in electronic structure theory: electric polarization, orbital magnetization and topological insulators* (Cambridge University Press, 2018).

[23] C. Fang, Y. Chen, H.-Y. Kee, and L. Fu, Topological nodal line semimetals with and without spin-orbital coupling, *Phys. Rev. B* **92**, 081201 (2015).

[24] T. Liu, J. J. He, Z. Yang, and F. Nori, Higher-order weyl-exceptional-ring semimetals, *Phys. Rev. Lett.* **127**, 196801 (2021).

[25] K. Kawabata, T. Bessho, and M. Sato, Classification of exceptional points and non-hermitian topological semimetals, *Phys. Rev. Lett.* **123**, 066405 (2019).

[26] T. Xia, X. Fan, Q. Chen, Y. Zhang, and Z. Li, A simple scheme to realize the rice-mele model in acoustic system, *Chinese Physics B* (2026).

[27] J. Kang, R. Wei, Q. Zhang, and G. Dong, Topological photonic states in waveguide arrays, *Advanced Physics Research* **2**, 2200053 (2023).

[28] S. Chen, A. Basit, L. Li, C. Hou, Y. Ruan, Y. Wei, and Z. Ni, Non-hermitian topological lattice photonics: An analytic perspective, *Advanced Photonics Research* **6**, 2500083 (2025).